The quadrupolar contribution to x-ray magnetic circular dichroism in REZn compounds

2008 J. Phys.: Condens. Matter 20 395217

(http://iopscience.iop.org/0953-8984/20/39/395217)

J. Phys.: Condens. Matter **20** (2008) 395217 (11pp) doi:10.1088/0953-8984/20/39/395217

The quadrupolar contribution to x-ray magnetic circular dichroism in REZn compounds

R-M Galéra[1], Y Joly[1], A Rogalev[2] and N Binggeli[3]

[1] Institut Néel, CNRS-UJF, BP 166, 38042 Grenoble Cedex 9, France
[2] European Synchrotron Radiation Facility, BP 220, F-38043 Grenoble Cedex 9, France
[3] Abdus Salam International Center for Theoretical Physics and CNR-INFM DEMOCRITOS National Simulation Center, Strada Costiera 11, 34014 Trieste, Italy

E-mail: rose-marie.galera@grenoble.cnrs.fr

Received 25 January 2008, in final form 12 August 2008
Published 1 September 2008
Online at stacks.iop.org/JPhysCM/20/395217

Abstract

X-ray magnetic circular dichroism experiments on REZn single crystals (RE = Gd, Tb, Dy, Ho and Er) performed at the rare-earth $L_{2,3}$ edges show important quadrupolar contributions whose final states are the empty 4f orbitals. Calculations of the dichroic spectra have been performed using first-principle calculations with a treatment of the 4f states based on the LSDA + U (LSDA: local spin density approximation) method and including the spin–orbit coupling. The good agreement between experimental and calculated spectra allows a detailed analysis of the quadrupolar and dipolar contributions to the experimental spectra at the rare-earth L edges. Complementary study of the Zn K edge in HoZn reveals the magnetism induced on the Zn atoms.

(Some figures in this article are in colour only in the electronic version)

1. Introduction

With the availability of efficient synchrotron radiation sources x-ray absorption spectroscopy techniques experience a successful development. A unique advantage of these techniques is to provide studies of electronic structures in complex systems with an element and orbital selectivity. Among these techniques the x-ray magnetic circular dichroism (XMCD) measures the difference between the absorption of left handed and right handed circularly polarized light by a system with a net magnetization [1]. XMCD is a promising tool to probe the magnetic polarization of a selected electronic shell. Indeed with the derivation of the sum rules it is possible to determine independently the orbital and spin moments of each shell [2]. Experimentally however, it rapidly turned out that at some edges the XMCD signal is not straightforwardly related to the magnetic polarization and that its interpretation is far more complex than expected. This is the case for instance at the $L_{2,3}$ edges of the rare-earths (RE) [3, 4]. At these edges the dipolar electric transition (E1) of the photo-induced electron allows probing the empty 5d states. In RE compounds these states play an important role in mediating the magnetic interaction. In pure RE metals or intermetallics the 5d states give rise, together with the 6s shell, to the conduction band and contribute to high density of states near the Fermi level. Moreover the 5d wavefunctions are extended enough to present a considerable overlap between neighboring sites. 5d states thus strongly contribute to the RKKY interactions between the local magnetic moment mainly borne by the open inner 4f shell. In gadolinium metal and many Gd-based intermetallics, the observed spontaneous magnetic moment is larger than the expected $7\mu_B$. This excess moment is generally attributed to spin-polarization of the conduction electrons and mainly to the 5d electron polarization. The observation of a non-negligible diffuse magnetic signal by polarized neutron diffraction in pure Gd is strongly consistent with this interpretation [5]. In RE-transition metal alloys the 3d–4f coupling is indirect involving two stages: the 3d–5d and 5d–4f interactions [6]. The rare-earth 5d band can hybridize with the 3d band of the allied transition metal. This may strongly affect the magnetic properties of the 3d metal with an onset of the 3d magnetism only above a critical concentration of the 3d metal,

as observed in the RE-Co and RE-Ni systems [7]. Probing the 5d states with XMCD is a valuable technique to get a deeper insight into the fundamental mechanism controlling the magnetic interactions in the rare-earth intermetallics.

The interpretation of the XMCD signal at the rare-earth $L_{2,3}$ edges has been dealt within a large number of experimental [3, 4, 8, 9] and theoretical works [10–15]. It is now well established that the XMCD spectra at the $L_{2,3}$ edges of rare-earths are not directly related to the spin density of the unoccupied 5d states, as drawn from the first single-particle model proposed by Schütz and co-workers [3], and that the spin-dependence of the matrix element of the E1 transition cannot be neglected for open 4f shell ions [11, 8]. In spite of that, the interpretation still remains matter of debate as recently stressed by Giorgetti *et al* [16]. Apparently the structures in the XMCD spectra may strongly depend on the rare-earth, the compound and even on the temperature as observed in $ErFe_2$. The value of the ratio L_2:L_3 of the XMCD signal is very often different from the statistical branching ratio, -1, given by the Fano factors. This suggests that the 5d band states bear an orbital momentum. The interpretation of the spectra is also hampered by the existence of structures arising from the quadrupolar contributions (E2). Since the very beginning, the contribution of electric quadrupole transitions has been taken into account in the interpretation of the x-ray resonant magnetic scattering (XRMS) phenomena at the rare-earth $L_{2,3}$ edges [17, 18]. As the spin-sensitive absorption is related to the imaginary part of the resonant scattering amplitude, it was rapidly pointed out that non-negligible quadrupolar contributions are present in x-ray magnetic dichroic phenomena at these edges [10]. In the XMCD spectra, features observed below the absorption edge are generally ascribed to these 2p–4f quadrupolar transitions. Unusually in $YbFe_2$, this E2 structure was reported to be in the middle of the dipolar signal at the Yb L_3 edge [19]. Moreover the balance between dipolar and quadrupolar contributions in the spectra cannot be straightforwardly quantified. Experimentally the E2 structures are quite well evidenced at the rare-earth L_3 edge, but barely resolved at the L_2 one [8]. In the first simulations of the XMCD spectra dipolar and quadrupolar parts were evaluated separately: the dipolar part from first-principle calculations, the quadrupolar one from atomic-multiplet calculations. The position in energy of the quadrupolar contribution was taken as an adjustable parameter [11]. More recently a similar approach, that calculates separately the E1 (cluster model calculation) and E2 (full-multiplet calculation) contributions has been developed by Asakura *et al* [15] to reproduce the XMCD spectra in the $R_2Fe_{14}B$ series. In this approach the relative intensity between E2 and E1 transitions was treated as an adjustable parameter. At the same time Wende *et al* [9] have proposed a new, but also indirect, procedure to extract the E2 contribution from the experimental XMCD spectrum. All these reasons make difficult the application of the magneto-optical sum rules at rare-earth $L_{2,3}$ edges.

XMCD studies at the rare-earth $L_{2,3}$ edges have been mainly performed on intermetallics where the allied 3d metal is magnetic [4, 16]. In these compounds the Fermi level lies in a region in energy where the rare-earth 5d states are strongly hybridized with the 3d states of the transition metal. The photo-electron is probing these hybridized states, then it is very likely that the magnetic character of the 3d metal has an influence on the XMCD spectra. This influence is however not easy to quantify. In the present study the Zn ions have a closed 3d shell, therefore the relevant hybridization is only with the unoccupied 4p states of Zn, weakly spin polarized. Effects due to the only rare-earth ion result from the local 4f–5d exchange, that generates the spin-dependent spectral weight [8]. When performed on systems where only the rare-earth is ferromagnetic, XMCD experiments were done on polycrystalline samples where the saturation of the magnetization is not always reached. Indeed, due to the anisotropy properties, the grains oriented at random often impede a magnetic saturation in low fields. It is worth noting that the saturation of the magnetization would insure a maximal XMCD signal and greatly help for a quantitative interpretation.

In the present paper we report on XMCD experiments carried out on oriented single crystals of rare-earth-zinc compounds at the RE $L_{2,3}$ absorption edges and also for the HoZn compound at the K edge of Zn. A systematic study has been performed on the heavy REZn as a whole that allows following the relative evolution of dipolar and quadrupolar contributions to the XMCD spectrum as function of the rare-earth. Numerical simulations of the XMCD spectra have been performed with the magnetic fdmnes code [21, 22]. This code, based on first-principle calculations, includes fully spin–orbit interactions and relativistic effects and thus allows treating the magnetic aspects in XANES and related spectroscopies. Different approaches, multiple scattering (MST) or finite-difference method (FDM), can be used to calculate the electronic structure of the probed materials. In the task of simulating the core spectroscopies, a main difficulty consists in the calculation of the final states of the photo-electron. Different approaches can be used depending on the absorbing atom and the probed edge. The atomic-multiplet approach is very successful when the final states are localized states e.g. at the $M_{4,5}$ edges of lanthanides and actinides or the $L_{2,3}$ edges of 3d transition metals. On the contrary at the K edge the mono-electronic approaches are quite well adapted to calculate the delocalized finals p states. In the present case both the delocalized 5d band states, through the E1 transition, and the highly localized 4f states, through the E2 transition, are reached by the photo-electron. First-principles methods have been faced with the difficulty of describing systems with strong Coulomb correlations as for instance the rare-earth ions. This is why the LSDA + U method has been developed [23]. Recently the LSDA + U approach has been used successfully to calculate x-ray resonant magnetic scattering (XRMS) and XMCD spectra at the $L_{2,3}$ edges of the rare-earth [24–26]. The calculations of the XMCD spectra reported in this work were all performed within the LSDA + U approach, they will be described in more details in the section 3.

In section 2 are reported the experimental details. The theoretical approach used for the calculation of the spectra and details about the calculation code are presented in section 3.

Table 1. Lattice parameter, Curie temperature, easy axis and spontaneous magnetization at 10 K in the heavy rare-earth compounds of the REZn series.

Compound	a (Å)	T_C (K)	Easy axis (10 K)	M_s (10 K) (μ_B)
GdZn	3.602	269	—	7.42
TbZn	3.576	200	[110]	8.93
DyZn	3.563	139	[001]	9.87
HoZn	3.547	75	[110]	8.35
ErZn	3.532	20	[001]	6.57

Section 4 deals with the analysis and comparison between calculations and experimental results. Preliminary results at the Zn K edge in HoZn are given in section 5 before to conclude.

2. Experimental details and results

2.1. Magnetic measurements

The REZn compounds crystallize in a simple cubic CsCl-type structure ($Pm3m$) that contains one atom of each specie by unit cell. They have been intensively studied as they turned out to be model systems for quadrupolar interactions and magneto-elastic effects [27]. In these compounds the Zn 3d shell is full and the magnetic properties come exclusively from the RE ions. Heavy rare-earth compounds order ferromagnetically with rather high Curie temperatures as shown in table 1. The samples used for XMCD measurements are spark-cut single crystalline disks of 7 mm diameter and 0.5–1 mm height. For each compound the disk surface was cut perpendicular to the easy magnetization axis at 10 K, the base temperature of the XMCD experimental set-up. Prior to XMCD experiments the magnetization processes of each sample were checked in the temperature range 2–20 K. The measurements were performed at the Institut Néel by the extraction method in fields up to 10 T. The sensitivity of these measurements reaches 5×10^{-7} Am^2. The magnetic field was applied along the easy axis i.e. perpendicular to the disk surface. The magnetization curves obtained at 10 K are reported in figure 1. For all samples the magnetization increases linearly with the field before to reach the saturation. This linear regime is associated with the domain wall motion that leads to the single domain phase at which the magnetization reaches its spontaneous value. The values of the spontaneous magnetization at 10 K reported in table 1 compare quite well with those previously reported by Morin *et al* [27]. Increasing the field a slight superposed susceptibility is observed in HoZn and ErZn. This superposed susceptibility becomes larger when the temperature of the measurements gets closer to the Curie temperature. The decrease of the Curie temperature from GdZn to ErZn is ascribed to the decrease of the 4f spin value (see table 2). For GdZn the spontaneous magnetization at 10 K is larger than the saturated 4f magnetic moment expected for the trivalent ion at 0 K (see table 2). As for pure Gd, this may be ascribed to the spin-polarization of the 5d conduction electrons. On the contrary for all the other compounds the spontaneous magnetization remains smaller than the expected saturated moment (table 2). This is due to the reduction of the magnetic moment by the crystalline electric field that acts on $L \neq 0$ RE ions [27].

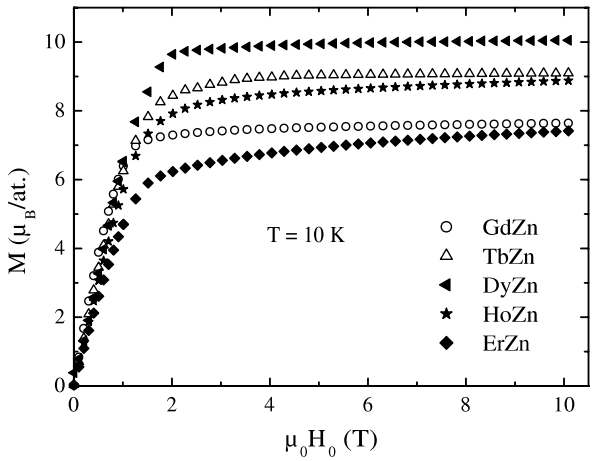

Figure 1. Magnetization processes at 10 K for the five studied REZn compounds. The magnetization is given in Bohr magneton per RE ion.

Table 2. Number of 4f electrons, values of the spin, orbital and total angular momenta for the ground multiplet of the trivalent heavy RE free ions. Columns six and seven give respectively the Lande factor and the saturated magnetic moment, $\mu_s = g_J J$.

RE ion	n_{4f}	S_{4f}	L_{4f}	J	g_J	μ_s (0 K) (μ_B)
Gd^{3+}	7	7/2	0	7/2	2	7
Tb^{3+}	8	3	3	6	3/2	9
Dy^{3+}	9	5/2	5	15/2	4/3	10
Ho^{3+}	10	2	6	8	5/4	10
Er^{3+}	11	3/2	6	15/2	6/5	9

2.2. XMCD measurements

The XMCD experiments have been carried out at the ESRF ID12 beamline optimized for polarization-dependent x-ray absorption fine structure studies [28]. The source of circularly polarized photons was the Helios II Undulator, which allows flipping the helicity of the photon beam after each energy scan. The incident energy is selected by a pair of Si⟨111⟩ crystals. In the energy range of the RE $L_{2,3}$ absorption edges, polarimetry experiments have found that the circular polarization rate is 88% [29]. The samples were mounted on the cold finger of a liquid-helium cryostat inserted in a superconducting cryomagnet. For all samples the experiments were performed at 10 K under a field of 3 T, applied along the easy magnetization axis. According to the magnetization curves in figure 1, under 3 T the samples are all in the single domain phase. In this configuration, the XMCD signal is expected to reach its maximum amplitude. All x-ray absorption near edge structure (XANES) spectra discussed in the present paper were collected in the total x-ray fluorescence detection mode. Due to well-known saturation/self-absorption effects, fluorescence yield spectra are not linearly proportional to x-ray absorption spectra. A rather simple homographic transform of the fluorescence data was systematically used to restore spectra

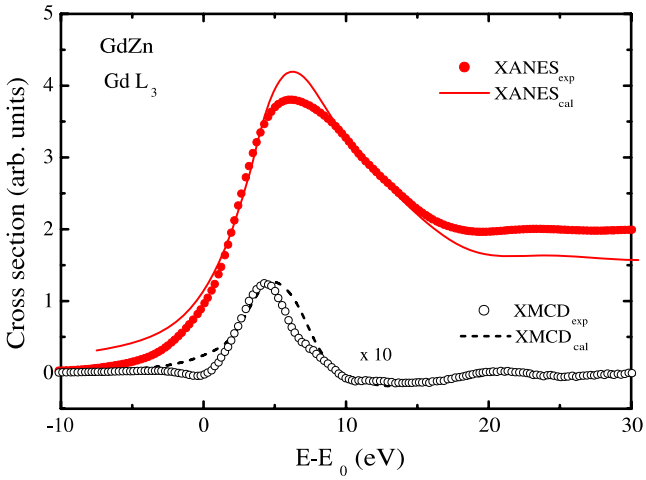

Figure 2. Calculated (full line) and experimental (full dots) XANES signals at the Gd L_3 edge in GdZn. The dotted line and open dots represent the calculated and experimental XMCD signals respectively. The experimental spectrum energy has been shifted by the electron binding energy $E_0 = 7243$ eV.

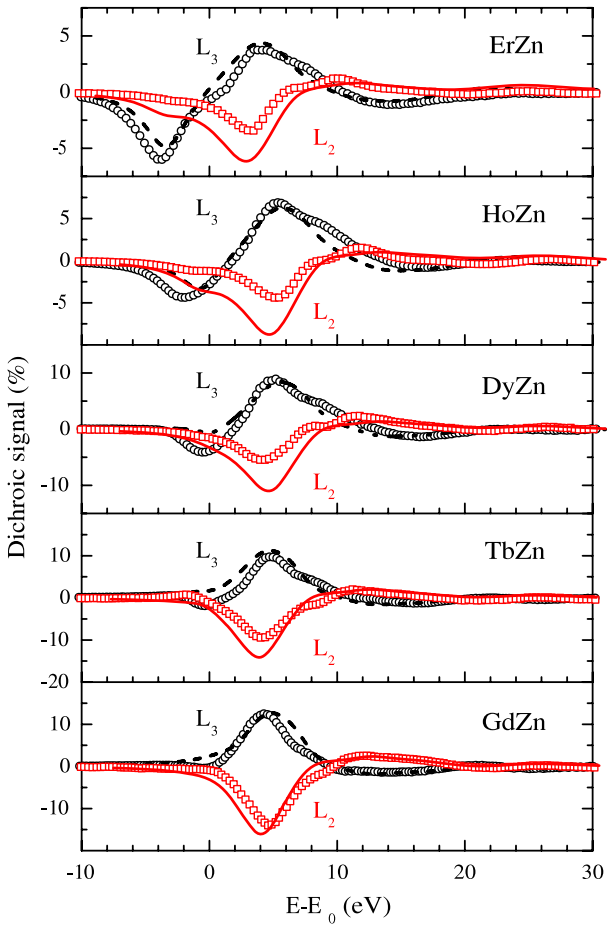

Figure 3. Calculated (full and dashed lines) and experimental (open dots and open diamonds) dichroic signals at the RE $L_{2,3}$ edges in the REZn series. At the L_3 edge, the increasing structure when going from Gd to Er, located in the lowest-energy part of the spectrum is definitively ascribed to the quadrupole–quadrupole (E2–E2) contribution. For all the spectra E_0 is the value of the tabulated electron binding energy for the respective edges [31].

proportional to the absorption coefficient (see [30]). XMCD spectra were obtained as a direct difference of the corrected XANES spectra recorded with opposite helicity of incoming x-rays. The convention adopted by all experimentalists is XMCD $= \sigma^{-(\text{right})} - \sigma^{+(\text{left})}$ with the magnetic field parallel to the wavevector of the photons. Before performing any normalization it was checked that for each rare-earth the L_3 absorption edge step is twice that at the L_2. Then the L_2 XANES spectra are normalized to the height of the absorption edge step while the L_3 ones are normalized to the half of the step height (see for instance figure 2). Within this normalization we recover the actual ratios 1:2 and −1:1 for the L_2:L_3 XANES and XMCD ratios respectively. The experimental XMCD spectra at the RE $L_{2,3}$ edges are reported in figure 3. To achieve a reliable comparison between calculated and experimental spectra and also to reduce the number of parameters it is important to define a commune origin in energy, E_0. In the present work the origin E_0 is the value of the tabulated electron binding energy for the selected edge [31]. From Gd to Er, experimental spectra show a progressive decrease of the signal centered around +5 eV, at both the L_3 and L_2 edges, while at the L_3 a positive structure increases in the lowest-energy part of the spectra.

3. Theory

3.1. Cross section and tensorial approaches

In a mono-electronic description, such as in the LSDA + U approach, the normalized atomic absorption cross section which stands as well for absorption or XMCD is given by:

$$\sigma = \sum_{fi} |\langle \psi_f | \hat{O} | \psi_i \rangle|^2 \delta(\hbar\omega - (E_f - E_i)) \qquad (1)$$

where ψ_i and ψ_f are respectively the ground and photo-excited states, $\hat{O}$ the interacting operator between the electromagnetic field and the material, $\hbar\omega$ the photon energy and $\delta(\hbar\omega - (E_f - E_i))$ the state density. In the following, this term will be included in the normalization of the final photo-excited state and thus will not appear anymore. The un-normalized cross sections contain an additional factor $4\pi^2\alpha\hbar\omega$, where α is the fine structure constant. The purpose of the present paper being a comparative study at the L_2 and L_3 edges, the normalized cross section is more convenient. Indeed, in absence of spin–orbit in the final state and of multi-electronic phenomena, the ratio L_2:L_3 of the XANES and of the XMCD spectra would have to be respectively 1:2 and −1:1, at least in the usually dominant dipole–dipole (E1–E1) channel [32].

In the present case there is only one atom of each chemical specie in the unit cell, thus no summation on atoms or symmetry operation must be added to the previous formula to get the unit mesh cross section. In the x-ray regime, the magnetic part of the electromagnetic field can be neglected and the operator $\hat{O}$ is reduced to its electric part. It is usually written through the multipolar expansion of this electric field

up to the quadrupole term:

$$\hat{O} = \vec{\epsilon} \cdot \vec{r} \left(1 - \tfrac{1}{2} \mathrm{i} \vec{k} \cdot \vec{r}\right) \tag{2}$$

where $\vec{r}$ is the electron position measured from the absorbing ion, $\vec{\epsilon}$ the polarization of the photon and $\vec{k}$ its corresponding wavevector.

The tensor approach is very useful to expand the formula of the cross section (equation (1)) on the Cartesian polarization and wavevector components:

$$\begin{aligned}\sigma = &\sum_{\alpha\beta} \epsilon^*_\alpha \epsilon_\beta D_{\alpha\beta} - \frac{\mathrm{i}}{2} \sum_{\alpha\beta\gamma} \epsilon^*_\alpha \epsilon_\beta k_\gamma (I_{\alpha\beta\gamma} - I^*_{\beta\alpha\gamma}) \\ &+ \tfrac{1}{4} \sum_{\alpha\beta\gamma\delta} \epsilon^*_\alpha \epsilon_\beta k_\gamma k_\delta Q_{\alpha\beta\gamma\delta}\end{aligned} \tag{3}$$

where α, β, γ and δ are Cartesian coordinate labels and $D_{\alpha\beta}$, $I_{\alpha\beta\gamma}$ and $Q_{\alpha\beta\gamma\delta}$, the dipole–dipole (E1–E1), dipole–quadrupole (E1–E2) and quadrupole–quadrupole (E2–E2) contributions, respectively. Their explicit expressions are given by:

$$\begin{aligned} D_{\alpha\beta} &= \sum_{fi} \langle \psi_i | r_\alpha | \psi_f \rangle \langle \psi_f | r_\beta | \psi_i \rangle \\ I_{\alpha\beta\gamma} &= \sum_{fi} \langle \psi_i | r_\alpha | \psi_f \rangle \langle \psi_f | r_\beta r_\gamma | \psi_i \rangle \\ Q_{\alpha\beta\gamma\delta} &= \sum_{fi} \langle \psi_i | r_\alpha r_\beta | \psi_f \rangle \langle \psi_f | r_\gamma r_\delta | \psi_i \rangle . \end{aligned} \tag{4}$$

The dipole–quadrupole (E1–E2) only probes the projection on the absorbing atoms of the hybridized odd–even states. Thus they are zero in the centro-symmetric materials of the present study.

To get the cross sections as a function of the atomic amplitudes, we first expand the initial and final states on spherical waves. For this we use the (ℓ, m, σ) basis where ℓ and m are the usual quantum numbers and σ stands for the spin. s is an index on the two independent solutions we get due to the complete treatment of the Dirac equation. Neglecting spin–orbit interaction s and σ could be merged, but here we keep the complete formulation, thus the initial and final states are given by:

$$\begin{aligned} \psi_i &= \sum_\sigma G^\sigma_i Y^{m_i+\sigma-\frac{1}{2}}_{\ell_i} g(r) \chi_\sigma \\ \psi_f &= \sum_{\ell m s} a^f_{\ell m s} \sum_\sigma Y^{m+\sigma-\frac{1}{2}}_\ell b^{\sigma s}_{\ell m+\sigma-\frac{1}{2}}(r) \chi_\sigma \end{aligned} \tag{5}$$

G^σ_i is a constant, χ_σ is the spin projection, $g(r)$ and $b^{\sigma s}_{\ell m+\sigma-\frac{1}{2}}(r)$ are the initial and final state radial functions. The $a^f_{\ell m s}$ are the amplitudes of the spherical harmonics of the different final states. They are calculated by continuity using any method of calculation providing the electronic structure of the material. In the field, the multiple scattering theory (MST) is certainly the most famous but any other method of calculation, in direct or reciprocal space, can be used as well. The $a^f_{\ell m s}$ contain all the information on the spin and electronic structure on the absorbing atom.

To be complete, one has also to expand the r_α or $r_\beta r_\gamma$ operators in the spherical base. We note these terms r_o, where o indexes any of the operator types. In this way we get:

$$r_o = \sum_{m_o} c^o_{\ell_o m_o} Y^{m_o}_{\ell_o} r^{\ell_o} \tag{6}$$

where ℓ_o is 1 and 2 for the E1 and E2 transitions respectively. Including the expressions (5) and (6) in the equation (4) we get the general form for any component $T_{oo'}$ of the Cartesian tensors:

$$\begin{aligned} T_{oo'} = &\sum_{m_o m_{o'}} c^o_{\ell_o m_o} c^{o'}_{\ell_{o'} m_{o'}} \sum_{i\sigma} \chi_\sigma (G^\sigma_i)^2 \\ &\times \sum_{\ell m \ell' m'} \Gamma\Gamma' \sum_{ss'} R^{\sigma s}_{\ell m} R^{\sigma s' *}_{\ell' m'} \sum_f a^f_{\ell m s} a^{f^*}_{\ell' m' s'} \end{aligned} \tag{7}$$

where Γ are the Gaunt coefficients and $R^{\sigma s}_{\ell m} = \langle b^{\sigma s}_{\ell m+\sigma-\frac{1}{2}}(r) | r^{l_o} | g(r) \rangle$ are the radial integrals. The optical theorem shows that the last part of the equation is nothing else than the imaginary part of the multiple scattering amplitude:

$$\sum_f a^f_{\ell m s} a^{f^*}_{\ell' m' s'} = -\mathrm{Im}(\tau^{\ell' m' s'}_{\ell m s}). \tag{8}$$

We will also use the spherical tensors which are more useful to express the measurements in term of observable. The spherical tensors can be calculated from the Cartesian ones. The general expression for the absorption cross section is then:

$$\begin{aligned} \sigma = &\sum_{\ell=0,2} (-1)^{\ell+m} P^m_\ell D^m_\ell \\ &+ \sum_{\ell=1,3} (-1)^{\ell+m} (P^m_\ell I^m_\ell + P^{m'}_\ell I^{m'}_\ell) \\ &+ \sum_{\ell=0,4} (-1)^{\ell+m} P^m_\ell Q^m_\ell \end{aligned} \tag{9}$$

where the first, second and third summations correspond to respectively the (E1–E1), (E1–E2) and (E2–E2) channels. D^m_ℓ, I^m_ℓ and Q^m_ℓ are the corresponding scattering tensors. P^m_ℓ is the polarization-wavevector tensor also expressed in the spherical bases. For the (E1–E2) channel the magnetic terms are separated from the electric ones. They are the tensors noted with a prime. For (E1–E1) and (E2–E2), $\ell = 0, 1, 2, 3$ and 4 corresponds respectively to the electric monopole, magnetic dipole, electric quadrupole, magnetic octupole and electric hexadecapole. We must stress that one shall not confuse the terms of 'dipole' and 'quadrupole' used here with the dipolar (E1) and quadrupolar (E2) electric transitions that correspond to the expansion in k of the photon electric field (see equation (2)). Equation (9) accounts for the non-isotropic scattering processes arising from the crystal anisotropy. At the K edge the magnetic dipole is a direct measurement of the density of the orbital magnetic moment (mainly carried by the p states). At the $L_{2,3}$ edges it is related in a more complex way to the density of the spin moment, the orbital moment and a third expectation value related to the anisotropy of the field of the spins. Nevertheless the sum over the $L_{2,3}$ edges is, as for the K edge, only proportional to the orbital magnetic moment of the d states, at least for the (E1–E1) transition [2]. Note

however that for the rare-earths, the difference in the spin-up and spin-down 5d radial functions makes that the ratio between the square of the modulus of the radial integral, $|R^{\sigma s}_{\ell m}|^2$, and $\langle b^{\sigma s}_{\ell m+\sigma-\frac{1}{2}}(r)|b^{\sigma s}_{\ell m+\sigma-\frac{1}{2}}(r)\rangle$, are different for spin-up and spin-down (the so-called 'breathing effect'). The consequence is that the sum rules at the $L_{2,3}$ edges of the rare-earths are not very precise to determine the 5d orbital moment. In the present work we calculate precisely the matrix elements but at the present stage our purpose was not the quantitative determination of the orbital moment of the final 5d states. It is worth noting that this determination is the main object of an unambiguous interpretation of the XMCD spectra. For the (E2–E2) channel, due to the more complex selection rule, the sum over the $L_{2,3}$ edges is proportional with different weights to the partial orbital magnetic moments.

In XMCD, the signal is the difference of the cross section between right (σ^-) and left (σ^+) polarizations. In the cubic ferromagnetic REZn compounds, quite all tensors are thus eliminated. Choosing the z axis along the spin direction one gets respectively for the XMCD and absorption cross sections:

$$\sigma^- - \sigma^+ = -\sqrt{2}D^0_1 - \frac{1}{\sqrt{10}}Q^0_1 + \sqrt{\frac{8}{35}}Q^0_3 \qquad (10)$$

$$\frac{1}{2}(\sigma^+ + \sigma^-) = \frac{1}{\sqrt{3}}D^0_0 + \frac{1}{\sqrt{20}}Q^0_0 - \sqrt{\frac{2}{35}}Q^0_4. \qquad (11)$$

The expression of the XMCD in equation (10) reduces to three terms, it follows that the XMCD can probe only few of the different physical parameters. The fact that the remaining terms correspond to the $m = 0$ projection of ℓ means that the z axis remain a symmetry axis. The summation over the L_2 and L_3 edges of the first term D^0_1 gives the projection along z of the magnetic orbital moment carried by the occupied 5d levels (with the limitation due to the breathing effect as noted above). The same summation of the second, Q^0_1, and third, Q^0_3, terms will give the projection of the 4f magnetic orbital moment and the 4f magnetic octupole respectively. The magnetic octupole is an expansion at higher order of the current around the absorbing atom. Note also that, due to the radial and angular integrals ($R^{\sigma s}_{\ell m}$ and Γ in equation (7)), a factor strongly different between the (E1–E1) and (E2–E2) channels, should be applied in order to get the magnetic moments in conventional units. From the absorption cross section defined by equation (11) it is possible to probe the isotropic (or monopole) (E1–E1) and (E2–E2) channels and the electric hexadecapole. This last contribution has been detected in pyrite, but at the iron K edge. Unfortunately, the very short hole lifetime in present experiments cannot allow a quantitative detection of this contribution.

3.2. Calculation of the final states

The calculations of the final states are performed using the local spin density approximation corrected by the Hubbard term (LSDA + U) to better account for the effects of the strong Coulomb interactions on the 4f rare-earth levels [23]. This correction cannot be neglected at the rare-earth $L_{2,3}$ edges because the final states of the quadrupolar transitions are the 4f empty states. At these edges however the important broadening makes that the detailed multi-electronic features are not visible in the experimental spectra. Nevertheless the position in energy of the quadrupolar component with respect to the dipolar one is an important issue and a good evaluation of this position requires the Hubbard correction. In the present study the effective on-site interaction parameter, $U_{\rm eff} = U - J$, was kept at 6 eV for all the rare-earth ions. This is a reasonable value for the 4f on-site exchange–correlation interactions in the corresponding rare-earth metals and alloys [23, 26, 33]. The typical U quoted for 4f is between 6 and 9 eV. Due to the experimental resolution, the intrinsic broadening and the fact that we work at the $L_{2,3}$ edges, far less sensitive than the $M_{4,5}$ ones, this value is adequate to reach a convenient agreement. A few cycles of calculations are sufficient to get the occupancy matrix, $\rho^{\sigma}_{mm'}$, of the different f levels, where σ stands for the spin and m and m' for the third atomic quantum number. In practice the choice of the convenient basis makes that only the diagonal terms ($m = m'$) are not zero. Following the Dudarev *et al* scheme [34], the correction induced by $U_{\rm eff}$ in the one-electron potential matrix of the 4f states is given by:

$$\Delta V^{\sigma}_{mm'} = U_{\rm eff}\left(\tfrac{1}{2}\delta_{mm'} - \rho^{\sigma}_{mm'}\right). \qquad (12)$$

The Fermi level is found inside the 'gap' opened by the Hubbard correction between the 4f states. The total electronic density being rather low within this region in energy the position of the Fermi level is obtained with an uncertainty of the order of 1 eV. Such an uncertainty may be a strong limitation when calculating some physical properties. In the present case however it does not affect the calculation of the dichroic spectra. It was checked that a quite good agreement between calculated and experimental spectra is reached following this procedure. Neglecting the Hubbard correction, instead, and seeking agreement with the experimental spectra by adjusting the occupation of the 4f levels would lead to a systematic overestimation by 0.2 electrons of the nominal number of 4f electrons for trivalent rare-earth ions. From the calculated electronic structure the XANES and XMCD cross sections are evaluated at any energy. As the photo-electron can reach only empty states, the calculated spectra reported in figures 2–4 and 6 are obtained by canceling the transitions to the occupied states before making the convolution.

3.3. Convolution

The formulae given in the previous chapter stand for complex potentials. Often it is more convenient to keep a real potential, and to account for the core-hole and final state lifetimes by a Lorentzian convolution afterward. The 4f levels being extremely narrow in energy, it is usual for numerical convenience to introduce a very small imaginary part to the energy (≈0.1 eV) to avoid an infinitely small energy grid of calculation. In a second step the usual convolution is performed. This later one is energy dependent: it increases from the edge where the values spread from 3.8 eV for gadolinium to 4.1 eV for erbium. At 40 eV above the edge, the width reaches typically 14 eV. A consequence of this relatively

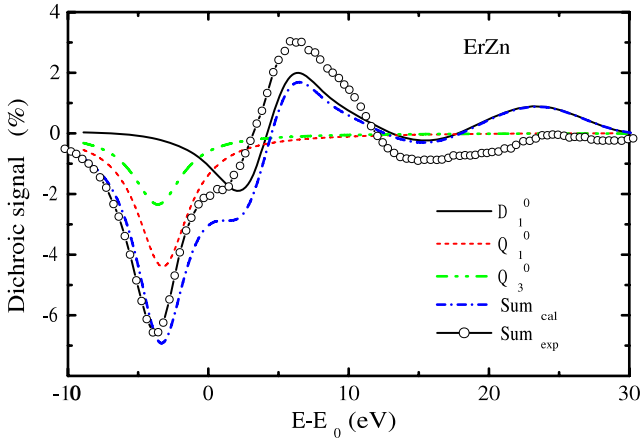

Figure 4. Summation over the L_2 and L_3 edges of the calculated (dash dot line) and experimental (open circles) dichroic signal in ErZn. The contribution of the different components, D_1^0 (solid line), Q_1^0 (dashed line) and Q_3^0 (dash dot dot line) to the calculated signal are also reported. The Q_1^0 component related to the 4f orbital magnetic moment along z, is the dominant contribution to the signal.

strong broadening is that an important part of the information is lost. Also taking into account properly this broadening is one of the difficulties in the present study. Care must be taken in the width determination because the XMCD spectra oscillate around the zero line, being alternatively positive and negative as function of the energy. Thus over or underestimations of the width lead consequently to a global XMCD signal itself under or overestimated. As it is not the case for the XANES spectra, the ratio between XMCD and XANES may be also affected. It is worth noting that the XMCD/XANES ratio should be respected.

3.4. About the calculation code

We have performed the numerical simulations with the *ab initio* magnetic code implemented in the fdmnes package [21, 22]. This code uses different approaches based on the multiple scattering theory (MST) or on the finite-difference method (FDM) to calculate the electronic structure of the involved materials. Magnetic effects are treated through a relativistic extension of the Schrödinger equation built without any approximation from the Dirac equation. Thus it includes fully spin–orbit interactions and relativistic effects [21]. It also includes now the Hubbard correction. The code also permits an analysis of the multipolar scattering tensors providing thus a useful information on the physical variables that give rise to the observed signal.

The cubic REZn compounds are highly symmetric and dense materials. In this case, non-muffin-tin effects are known to be small, thus the MST approach, which uses the muffin-tin approximation for the shape of the potential can be preferred to the FDM. Indeed, the MST approach is more economical and permits calculations with bigger clusters. It has been checked that both methods of calculation, the MST and the FDM, give close results. For all compounds clusters of 8 Å radius were used. They include more than 110 atoms and the convergence is then perfectly achieved. The specific parameters in the muffin-tin approximation: the atomic sphere radius and the interstitial potential, were calculated in the same way for all compounds, thus avoiding extra and dangerous parameters. The interstitial potential is chosen as the average potential between the atomic spheres. The atomic sphere radii were chosen in order to minimize the potential jumps between the different areas of calculation and with a 10% overlap.

4. Analysis of the rare-earth $L_{2,3}$ edges

4.1. Comparison with experiment

For each compound, the normalization between experiment and calculation is carried out in order to equalize the calculated XANES spectra at 30 eV above the edges. At this energy the XANES signal at the L_3 edge is twice as large as the one at the L_2 edge. Note that accordingly the origin of the energy for calculated XANES spectra is taken at beginning of the absorption edge in order to coincide with the origin of the experimental energy. The same normalization factor is thus applied to both the XMCD and XANES signals. Figure 2 gives an illustration of this normalization procedure at the Gd L_3 edge in GdZn. It is worth noting that this normalization allows comparing the XMCD amplitude between the different compounds. Calculated and experimental XMCD spectra are compared in the figure 3. At each absorption edge the amplitude and the evolution of the dichroic signal as function of the rare-earth are reproduced with a very satisfying agreement. Calculations account well for the decrease of the main amplitude around 5 eV when going from gadolinium to erbium. In the whole energy range the differences in shape between the L_2 and L_3 edges are also nicely reproduced. At the L_3 edge, the progressive rising of the structure at the lowest-energy part is well reproduced with a particularly good quantitative agreement for the Ho and Er compounds. Calculations confirm that this structure is strictly of (E2–E2) origin and thus probes the 4f states.

As shown in figure 3 the L_2:L_3 XMCD ratios are very far from the theoretical statistical branching ratio value, -1, that does not take into account the spin–orbit and multi-electronic phenomena. Present calculations account for the spin–orbit coupling and for the on-site correlations and electronic interaction effects but not for the interaction with the core-hole. The good agreement between experiments and calculations emphasizes the role of the spin–orbit at the L edges of the rare-earth. This result is fully consistent with the recent work by Kim *et al* [32] that points out the key role of the spin–orbit coupling in the 5d band in accounting for the L_2:L_3 experimental branching ration in both the XRMS and the XMCD.

4.2. Magnetic moment analysis

It was shown in section 3 that XMCD probes the magnetic moments, spin and/or orbital moments, carried by the selected electronic shell of the absorbing atom. For the ErZn compound we compare in figure 4 the summation over the $L_{2,3}$ edges of the three tensors, D_1^0, Q_1^0 and Q_3^0 with that of the experimental XMCD signal. A quite good agreement is again observed

between calculation and experiment. figure 4 brings a clear confirmation of the (E2–E2) origin of the XMCD signal in the lowest-energy part of the spectrum at the $L_{2,3}$ edges in ErZn. Quantitatively, the Q_1^0 contribution, that is the partial 4f orbital magnetic moment along the easy spin direction, is 2 times larger than the 4f magnetic octupole Q_3^0. The integral over the energy of D_1^0 gives the total orbital moment of the Er 5d level. This integral is close to zero.

Due to the selection rules and the different values of the corresponding factors, the Q_1^0 contribution for the (E2–E2) channel, which is the dominant one, is related to the individual density of the 4f orbital moments with different weights on the different orbitals. It is not exactly proportional to the total density of orbital moment as it is in the (E1–E1) channel. For example the orbital moment of the $m = \pm 3$ orbitals is not accessible at all. Thus, the quantitative interpretation of the measurement in term of orbital moment remains tricky. Anyway, starting from the equations (7) and (8), neglecting the energy overlap between the spin-up and spin-down states (what is close to the truth in the present case) and using the known values of the different Clebch–Gordon factors we can reach to simple new formula. For this we also consider that the imaginary part of the multiple scattering amplitudes is proportional to the density of state ρ_m^σ where $\sigma = \uparrow$ or $\downarrow$ stands for the spin. Then, considering only the 4f states one gets for the XMCD signal at the L_2 and L_3 edges:

$$\sigma_{L2} \propto 10\rho_{-2}^{\uparrow} + 4(\rho_{-1}^{\uparrow} - \rho_1^{\uparrow}) - 3\rho_0^{\uparrow} - 10\rho_2^{\downarrow} + 4(\rho_{-1}^{\downarrow} - \rho_1^{\downarrow}) + 3\rho_0^{\downarrow} \quad (13)$$

$$\sigma_{L3} \propto 5\rho_{-2}^{\uparrow} - 15\rho_2^{\uparrow} + 8(\rho_{-1}^{\uparrow} - \rho_1^{\uparrow}) + 3\rho_0^{\uparrow} + 15\rho_{-2}^{\downarrow} - 5\rho_2^{\downarrow} + 8(\rho_{-1}^{\downarrow} - \rho_1^{\downarrow}) - 3\rho_0^{\downarrow}. \quad (14)$$

Thus for the sum over the 2 edges one gets:

$$\sigma_{L2} + \sigma_{L3} \propto 15(\rho_{-2}^{\uparrow} + \rho_{-2}^{\downarrow}) + 12(\rho_{-1}^{\uparrow} + \rho_{-1}^{\downarrow}) - 12(\rho_1^{\uparrow} + \rho_1^{\downarrow}) - 15(\rho_2^{\uparrow} + \rho_2^{\downarrow}). \quad (15)$$

The combined spin–orbit and cluster effects make that the different $|m, \sigma\rangle$ 4f states are spread and these equations cannot be simplified. Also equations (13) and (14) show that the $m = \pm 3$ levels are not probed by the dichroic measurements at both the L_2 and L_3 edges. In absence of spin–orbit coupling, the different ρ_m^σ stand at the same energy for each spin σ, these equations simplify to the classical ones easy to exploit to get the total moment. Then one gets for the dichroic signal at the L_2 and L_3 edges:

$$\sigma_{L2} \propto \rho^{\uparrow} - \rho^{\downarrow} \quad (16)$$

$$\sigma_{L3} \propto -\rho^{\uparrow} + \rho^{\downarrow} \quad (17)$$

where ρ^σ is now the total density of state for the spin σ. If equations (16) and (17) apply one would observe the same Q_1^0 contribution at the L_2 and L_3 edges but with opposite sign. This is never the case even for GdZn where the total orbital moment of the Gd is zero and for which the density of empty 4f states is maximum. Indeed for this compound the quadrupolar contribution vanishes as shown in figure 3. Actually, as it will be shown in the following, the spin–orbit cannot be neglected as the dichroic signal depends on the spin–orbit coupling at each energy in the empty states. This is illustrated in figure 5 where are reported the partial densities of states of the 4f orbitals around the Fermi level for GdZn and ErZn. Depending on the quantum number m, the 4f levels are spread in each sub-band. At the higher-energy stands the $|-3, \downarrow\rangle$ level, then decreasing the energy come $|-2, \downarrow\rangle$, $|-1, \downarrow\rangle$, and so on. In GdZn the exchange–correlation splitting between occupied spin-up and unoccupied spin-down 4f orbitals is found of the order of 11 eV in fully consistency with previous results [23, 33]. For heavier rare-earths the 4f levels are spread in a more complex way because the Fermi level stands within the down states. In ErZn for instance the gap opened by the Hubbard term in the spin-down orbitals is of the order of 6 eV. In a schematic view the Hubbard correction yields a shift of $\approx -U/2$ for the occupied spin-down states and $\approx +U/2$ for the unoccupied ones.

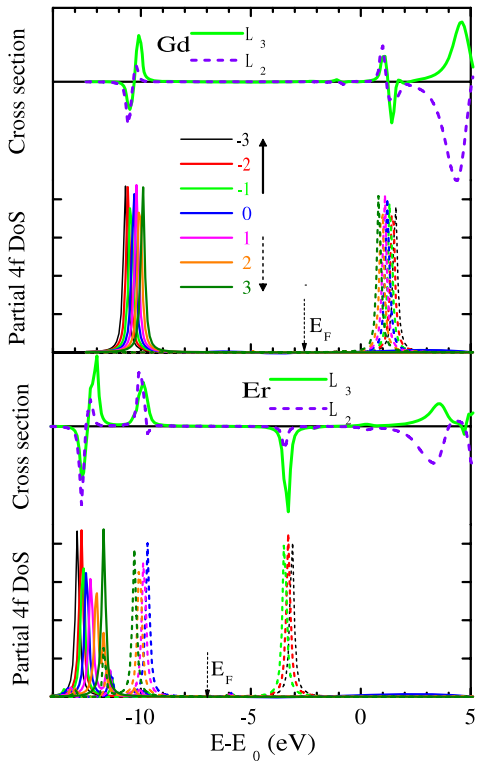

Figure 5. ErZn and GdZn compounds: lower part, partial density of states for the 4f orbitals. The spin–orbit coupling spreads the different 4f states, while the Hubbard correction splits the occupied and unoccupied states. The exchange–correlation splitting value is ≈11 eV and ≈6 eV for Gd and Er respectively. The Fermi level is found inside this gap its position is shown by an arrow. Upper part, dichroic cross section for the (E2–E2) and (E1–E1) processes calculated for all the finals states at the L_2 (dashed lines) and L_3 (solid lines) edges. The final spectra reported in the other figures are obtained by canceling first the transitions towards the occupied states beneath the Fermi level and second making the convolution.

The XMCD probes only the states above E_F which, for the studied compounds, are spin-down states. In GdZn these states are spread, from $m = 3$ to -3, within a thin energy range (≈1 eV). As shown in figure 5 (according to equations (13) and (14)) some m states give a positive contribution to the XMCD cross section, while others give a negative one. This finally results in an oscillatory theoretical curve as function

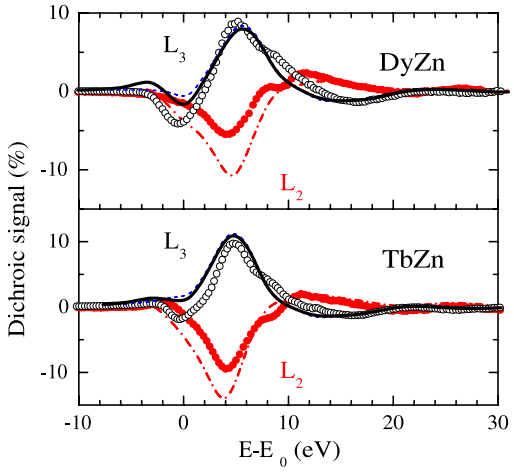

Figure 6. TbZn and DyZn compounds: calculated (full and dot dashed lines) and experimental (open and full dots) dichroic signals at the RE $L_{2,3}$ edges. The calculations have been performed assuming an overlap of 50% between the $|3,\downarrow\rangle$ and $|2,\downarrow\rangle$ orbitals and the $|2,\downarrow\rangle$ and $|1,\downarrow\rangle$ orbitals for Tb and Dy respectively. At the L_3 edge, it is compared with the calculation assuming the nominal occupation of the 4f orbitals (dashed line). At the L_2 edge not perceptible difference is observed between both calculations.

of the energy at both the L_2 and L_3 edges. To reproduce the experimental spectra it is necessary to account for an important broadening of the structures mainly due to the core-hole lifetime (≈3.8 eV). The convolution for GdZn makes that the positive and negative parts collapse leading to a very small final signal. In ErZn only the $|-3,\downarrow\rangle$, $|-2,\downarrow\rangle$ and $|-1,\downarrow\rangle$ levels are unoccupied (see figure 5). Thus the XMCD signal is quite only due to the moment brought by the $|-2,\downarrow\rangle$ and $|-1,\downarrow\rangle$ orbitals. At the L_3 edge according to equation (14) the signal becomes maximum because both contributions add and have a big coefficient. Despite the broadening a strong quadrupolar contribution to the XMCD is visible. At the L_2 on the contrary the $|-2,\downarrow\rangle$ does not contribute (see equation (13)) explaining the very small (E2–E2) effect at this edge. Now when decreasing Z, that is emptying the 4f orbitals, the $|0,\downarrow\rangle$ then the $|1,\downarrow\rangle$ and so on progressively contribute. These terms have the opposite sign (see equations (13) and (14)) and subtract to the previous contributions, consequently the signal decreases. From these considerations we can understand the evolution of the (E2–E2) contribution in the spectra. Coming back to figure 3 it can be seen that for TbZn, the (E2–E2) structure calculated at the L_3 edge is less pronounced than the experimental observation. For the Tb the last occupied level is the $|3,\downarrow\rangle$ orbital. According to equations (13) and (14), the $m = \pm 3$ levels do not intervene in the XMCD signal thus calculations lead to the same E2 contribution than for Gd, that actually is not observed. Assuming an overlap between the last occupied and first non-occupied nominal levels (for instance the $|3,\downarrow\rangle$ and $|2,\downarrow\rangle$ orbitals in Tb) the (E2–E2) structure can be calculated more intense and the agreement between the calculated and experimental spectra improved. This is illustrated in figure 6 for Tb and Dy. That best results are obtained for an occupation of the 4f orbitals different from the nominal one is quite surprising. Rather than an artifact this can be a consequence of the interaction with the core-hole during the absorption process.

To be complete, one also has to mention another parameter which perturbs the direct comparison between the L_2 and L_3 edges. The (E2–E2) signal being proportional to the square of the photon wavevector, an extra factor equal to the square of the ratio of the photon energy at the L_3 and L_2 edges must be considered. This factor is around 1.2 for the present rare-earth. It is not a true problem in the present study because the (E2–E2) contribution in the L_2 edge remains very small.

The strength of the (E1–E1) signal around 5 eV, at both the L_2 and L_3 thresholds, reflects the spin-polarization of the unoccupied 5d states. In the REZn compounds, these states are conduction states and their polarization results from the local 4f–5d exchange. The progressive decrease, when increasing Z, of the (E1–E1) signal is fully in agreement with the decrease of the 4f spin (see table 2). One may remark that for this dipole transitions the L_3:L_2 branching ratio of our experimental data has a quite different trend than the ones reported in references [12, 24, 32]. Actually the origin of such a difference remains unknown. Though the L_2 XMCD signal is calculated systematically larger than the experimental one, the simulated XMCD spectra account well for the overall trend of the dipolar part of the experimental spectra.

It is quite surprising that such a good agreement between experiment and calculation is obtained with a relatively simple fully relativistic LSDA + U approach. Indeed as soon as highly localized 4f states are involved more complex approaches are in principal required to take into account the interaction with the core-hole. Paradoxically this is due to the fact that the photo-electron probes an excited environment. In absence of a complete theory including multi-electronic and multi-atomic phenomena for x-ray absorption spectroscopy, and according to the fact that the interaction between the core and final states is less strong at the $L_{2,3}$ edges than at the $M_{4,5}$ ones, most of the core-hole effects can be simulated by the calculation of a self-consistent atomic potential for the absorbing atom (this one is then embedded in the total potential) and by a wide broadening that accounts for its short lifetime. Consequently the details due to the 4f states are visible neither in the experimental spectra nor in the simulations. Nevertheless, the simulation reproduces very well the trend of the spectra when changing the rare-earth. Thus the scheme of the spreading of the different 4f levels versus the quantum number m must be globally true. The fact that, using a fully relativistic LSDA + U approach, to calculate the XMCD at the rare-earth $L_{2,3}$ edges gives a satisfactory agreement is for us an interesting result by itself. Note also that the present approach handles both the dipolar and quadrupolar contributions on all the XANES energy range with satisfactory relative amplitudes between these channels. It also gives directly the position of the (E2–E2) contribution below the energy of the main dipolar one. Quadrupolar transitions to localized states arising at lower energy than dipolar transitions, is a general fact reproduced by the mono-electronic approach with no need of extra parameter. It is also true at the K edge of the 3d elements. In previous works, that use the multiplet approach to account for the (E2–E2) contribution, the position of the E2 peak relative to the E1 peak was treated as an adjustable parameter [11].

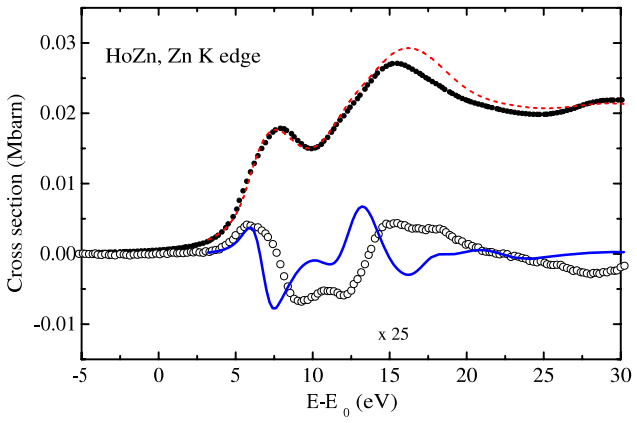

Figure 7. Calculated (dashed and full lines) and experimental (full and open dots) XANES and XMCD spectra at the Zn K edge in HoZn. The XMCD spectra are multiplied by 25. The calculated one has been further multiplied by 5 in order to be comparable to the experimental one.

5. Calculation of the zinc K edge in HoZn

Complementary measurements were performed at the K edge of Zinc in HoZn. At the K edge XMCD probes the polarization of the unoccupied p states of the selected element. Because there is no spin–orbit in the 1s initial state, the observed XMCD signal is due only to the spin–orbit coupling in the final p states. Consequently the XMCD signal at this edge is far smaller than at the $L_{2,3}$ edges. Despite the fact that the Zn 4p states are very delocalized conduction states and that the Zn ions bear no intrinsic magnetic moment (the Zn 3d shell is completely filled up), a non-negligible and structured signal is measured at the Zn K edge in HoZn (see figure 7). A previous work performed on rare-earth–cobalt intermetallics, had stressed the significant contribution of the 5d states of the rare-earth to the XMCD signal at the K edge of magnetic Co [35]. The present observation at the K edge of a non-magnetic element clearly confirms these first results. Simulations of the XANES and XMCD signals have been performed starting from the same initial conditions and with the same convolution procedure than for the simulations at the $L_{2,3}$ edges. The normalization between experiment and calculation was carried out in the same way than at the rare-earth L edges. Figure 7 shows a global agreement between the experimental and calculated XANES spectra. For clarity, the XMCD spectra are multiplied by 25 in figure 7. The calculated XMCD signal is five times smaller than the experimental one, in the figure it has been multiplied by this supplementary factor. The structures just above the edge are rather well reproduced by the calculation but the agreement becomes unsatisfactory at higher energies. As said before the convolution width is of crucial importance for a good simulation of the spectra, thus some discrepancies may partly be removed by optimizing it. However at this stage the factor 5 between the calculated and experimental dichroic spectra is not understood.

6. Conclusion

Experimental and theoretical studies of the XMCD have been performed at the $L_{2,3}$ thresholds of the rare-earth in the REZn compounds. The XANES and XMCD spectra have been calculated with the *ab initio* fdmnes code. This code allows accounting for the relativistic effect and especially for the spin–orbit coupling. The potential has been calculated within the muffin-tin approach and clusters of more than 110 atoms have been used. At the $L_{2,3}$ edges the simulations compare remarkably well with the experimental spectra. The analysis of the multipolar scattering tensors brings a quantitative evidence of the origin, (E1–E1) or (E2–E2), of the different features in the spectra. At the L_3 edge our study unambiguously confirms the (E2–E2) origin of the positive structure observed just at the edge. It explains also why this (E2–E2) contribution is less intense at the L_2 edge. The results obtained at the Zn K edge in HoZn are less satisfactory at least for the XMCD spectrum. The fact that the calculated signal is 5 times smaller than the experimental one is still an open question. This points out the difficulties encountered in theoretical approach when accounting for very delocalized conduction states.

Acknowledgments

One of the authors is very grateful to M Taillefumier and B Canals for their kind assistance. We acknowledge support for this work by the Light Source Theory Network, LighTnet, of the EU.

References

[1] Schütz G, Wagner W, Wilhelm W, Kienle P, Zeller R, Frahm R and Materlik G 1987 *Phys. Rev. Lett.* **58** 737
[2] Thole B T, Carra P, Sette F and van der Laan G 1992 *Phys. Rev. Lett.* **68** 1943
Altarelli M 1993 *Phys. Rev.* B **47** 597
Carra P, Thole B T, Altarelli M and Wang X 1993 *Phys. Rev. Lett.* **70** 694
[3] Schütz G, Knülle M, Wienke R, Wilhelm W, Wagner W, Kienle P and Frahm R 1988 *Z. Phys.* B **73** 67
[4] Fischer P, Schütz G and Wiesinger G 1990 *Solid State Commun.* **76** 777
Fischer P, Schütz G, Stähler S and Wiesinger G 1991 *J. Appl. Phys.* **69** 6144
Fischer P, Schütz G, Scherle S, Knülle M, Stähler S and Wiesinger G 1992 *Solid State Commun.* **82** 857
[5] Moon R M, Koehler W C, Cable J W and Child H R 1972 *Phys. Rev.* B **5** 997
[6] Campbell I A 1972 *J. Phys. F: Met. Phys.* **2** L47
[7] Gignoux D and Schmitt D 1995 *Handbook on the Physics and Chemistry of Rare Earths* ed K A Gschneidner Jr and L Eyring (Amsterdam: Elsevier) p 293
[8] Lang J C, Kycia S W, Wang X D, Harmon B N, Goldman A I, Branagan D J, McCallum R W and Finkelstein K D 1992 *Phys. Rev.* B **46** 5298
Lang J C, Wang X D, Antropov V P, Harmon B N, Goldman A I, Wan H, Hadjipanayis G C and Finkelstein K D 1994 *Phys. Rev.* B **49** 5993
Lang J C, Srajer G, Detlefs C, Goldman A I, König H, Wang X, Harmon B N and McCallum R W 1995 *Phys. Rev. Lett.* **74** 4935

[9] Wende H, Li Z, Scherz A, Ceballos G, Baberschke K, Ankudinov A, Rehr J J, Wilhelm F, Rogalev A, Schlagel D L and Lograsso T A 2002 *J. Appl. Phys.* **91** 7361
[10] Carra P and Altarelli M 1990 *Phys. Rev. Lett.* **64** 1286
Carra P, Harmon B N, Thole B T, Altarelli M and Sawatzky G A 1991 *Phys. Rev. Lett.* **66** 2495
[11] Wang X, Leung T C, Harmon B N and Carra P 1993 *Phys. Rev.* B **47** 9087
[12] van Veenendaal M, Goedkoop J B and Thole B T 1997 *Phys. Rev. Lett.* **78** 1162
[13] Matsuyama H, Harada I and Kotani A 1997 *J. Phys. Soc. Japan* **66** 337
[14] Fukui K, Ogasawara H, Kotani A, Harada I, Maruyama H, Kawamura N, Kobayashi K, Chaboy J and Marcelli A 2001 *Phys. Rev.* B **64** 104405
[15] Asakura K, Nakahara J, Harada I, Ogasawara H, Fukui K and Kotani A 2002 *J. Phys. Soc. Japan* **71** 2771
[16] Giorgetti Ch, Dartyge E, Baudelet F and Galéra R M 2004 *Phys. Rev.* B **70** 035105
[17] Gibbs D, Harshman D R, Isaacs E D, McWhan D B, Mills D and Vettier C 1988 *Phys. Rev. Lett.* **61** 1241
Hannon J P, Trammell G T, Blume M and Gibbs D 1988 *Phys. Rev. Lett.* **61** 1245
[18] Carra P, Altarelli M and de Bergevin F 1989 *Phys. Rev.* B **40** 7324
[19] Giorgetti Ch, Dartyge E, Brouder Ch, Baudelet F, Meyer C, Pizzini S, Fontaine A and Galéra R M 1995 *Phys. Rev. Lett.* **75** 3186
[20] Galéra R M, Pizzini S, Blanco J A, Rueff J P, Fontaine A, Giorgetti Ch, Baudelet F, Dartyge E and López M F 1995 *Phys. Rev.* B **51** 15957
[21] Joly Y 2001 *Phys. Rev.* B **63** 125120
Joly Y, Di Matteo S and Natoli C R 2004 *Phys. Rev.* B **69** 224401
[22] The fdmnes program can be downloaded at the web address http://www.neel.cnrs.fr/fdmnes
[23] Anisimov V I, Aryasetiawan F and Lichtenstein A I 1997 *J. Phys.: Condens. Matter* **9** 767
[24] Lee Y, Kim J-W, Goldman A I and Harmon B N 2005 *J. Appl. Phys.* **97** 10A311
[25] Yaresko A, Perlov A, Antonov V and Harmon B 2006 *Magnetism: a Synchrotron Radiation Approach* (*Lecture Notes in Physics* vol 697) (Berlin: Springer) p 121
[26] Antonov V N, Harmon B N, Yaresko A N and Shpak A P 2007 *Phys. Rev.* B **75** 184422
[27] Morin P, Rouchy J and du Tremolet de Lacheisserie E 1977 *Phys. Rev.* B **16** 3182
Morin P and Schmitt D 1990 *Ferromagnetic Materials* vol 5 ed K H J Buschow and E P Wohlfarth (Amsterdam: Elsevier Science) p 1
[28] Rogalev A, Goulon J, Goulon-Ginet C and Malgrange C 2001 *LNP: Magnetism and Synchrotron Radiation* (*Lecture Notes in Physics* vol 565) ed E Beaurepaire, F Scheurer, G Krill and J-P Kappler (Berlin: Springer) p 60
[29] Varga L, Giles C, Neumann C, Rogalev A, Malgrange C, Goulon J and de Bergevin F 1997 *J. Physique Coll.* IV **C2** 309
[30] Goulon J, Goulon-Ginet C, Cortés R and Dubois J M 1982 *J. Phys.* **43** 539
[31] Bearden J A and Burr A F 1967 *Rev. Mod. Phys.* **39** 125
[32] Kim J W, Lee Y, Wermeill De, Sieve B, Tan L, Bud'ko S L, Law S, Canfield P C, Harmon B N and Goldman A I 2005 *Phys. Rev.* B **72** 064403
[33] Shick A B, Pickett W E and Fadley C S 2000 *J. Appl. Phys.* **87** 5878
[34] Dudarev S L, Botton G A, Savrasov S Y, Humphreys C J and Sutton A P 1998 *Phys. Rev.* B **57** 1505
[35] Rueff J P, Galéra R M, Giorgetti Ch, Dartyge E, Brouder Ch and Alouani M 1998 *Phys. Rev.* B **58** 12271